

Learned, Uncertainty-driven Adaptive Acquisition for Photon-Efficient Multiphoton Microscopy

CASSANDRA TONG YE¹, JIASHU HAN², KUNZAN LIU¹, ANASTASIOS ANGELOPOULOS³, LINDA GRIFFITH⁴, KRISTINA MONAKHOVA^{1*}, SIXIAN YOU^{1*}

¹*Research Laboratory of Electronics (RLE) in the Department of Electrical Engineering and Computer Science, Massachusetts Institute of Technology*

²*Fu Foundation School of Engineering and Applied Science, Columbia University in the City of New York*

³*Department of Electrical Engineering and Computer Science, University of California, Berkeley*

⁴*Department of Biological Engineering, Massachusetts Institute of Technology*

*Sixian You: sixian@mit.edu

Kristina Monakhova: monakhova@cornell.edu

Abstract:

Multiphoton microscopy (MPM) is a powerful imaging tool that has been a critical enabler for live tissue imaging. However, since most multiphoton microscopy platforms rely on point scanning, there is an inherent trade-off between acquisition time, field of view (FOV), phototoxicity, and image quality, often resulting in noisy measurements when fast, large FOV, and/or gentle imaging is needed. Deep learning could be used to denoise multiphoton microscopy measurements, but these algorithms can be prone to hallucination, which can be disastrous for medical and scientific applications. We propose a method to simultaneously denoise and predict pixel-wise uncertainty for multiphoton imaging measurements, improving algorithm trustworthiness and providing statistical guarantees for the deep learning predictions. Furthermore, we propose to leverage this learned, pixel-wise uncertainty to drive an adaptive acquisition technique that rescans only the most uncertain regions of a sample. We demonstrate our method on experimental noisy MPM measurements of human endometrium tissues, showing that we can maintain fine features and outperform other denoising methods while predicting uncertainty at each pixel. Finally, with our adaptive acquisition technique, we demonstrate a 120× reduction in acquisition time and total light dose while successfully recovering fine features in the sample. We are the first to demonstrate distribution-free uncertainty quantification for a denoising task with real experimental data and the first to propose adaptive acquisition based on reconstruction uncertainty.

1. Introduction

Multiphoton microscopy (MPM) is a form of laser-scanning microscopy based on nonlinear interactions between ultrafast laser pulses and biological tissues. Since its first demonstration decades ago [1], MPM has become the imaging technique of choice for non-invasive imaging of thick or living samples [2, 3]. Owing to its unique advantage of imaging depth and subcellular resolution, MPM has been used extensively to measure calcium dynamics in deep scattering mouse brains in neuroscience and characterizing multicellular dynamics in immunology and cancer studies [4–7]. In addition, label-free MPM enables minimally invasive imaging of biological structures in living and unlabeled biosystems, such as collagen fibers, immune cells, endothelial cells, and extracellular vesicles [8], through second harmonic generation (SHG) [9], third harmonic generation (THG) [10, 11], and two-photon and three-photon autofluorescence [12]. Because of these unique advantages of MPM, it has made tremendous progress and become an increasingly popular tool for tissue and cell microscopy in neuroscience, immunology, and cancer research [13–17].

To provide a minimally perturbative window into the tissue architecture and cell dynamics of intact biosystems, the next advances in MPM require deeper, faster, and gentler imaging of

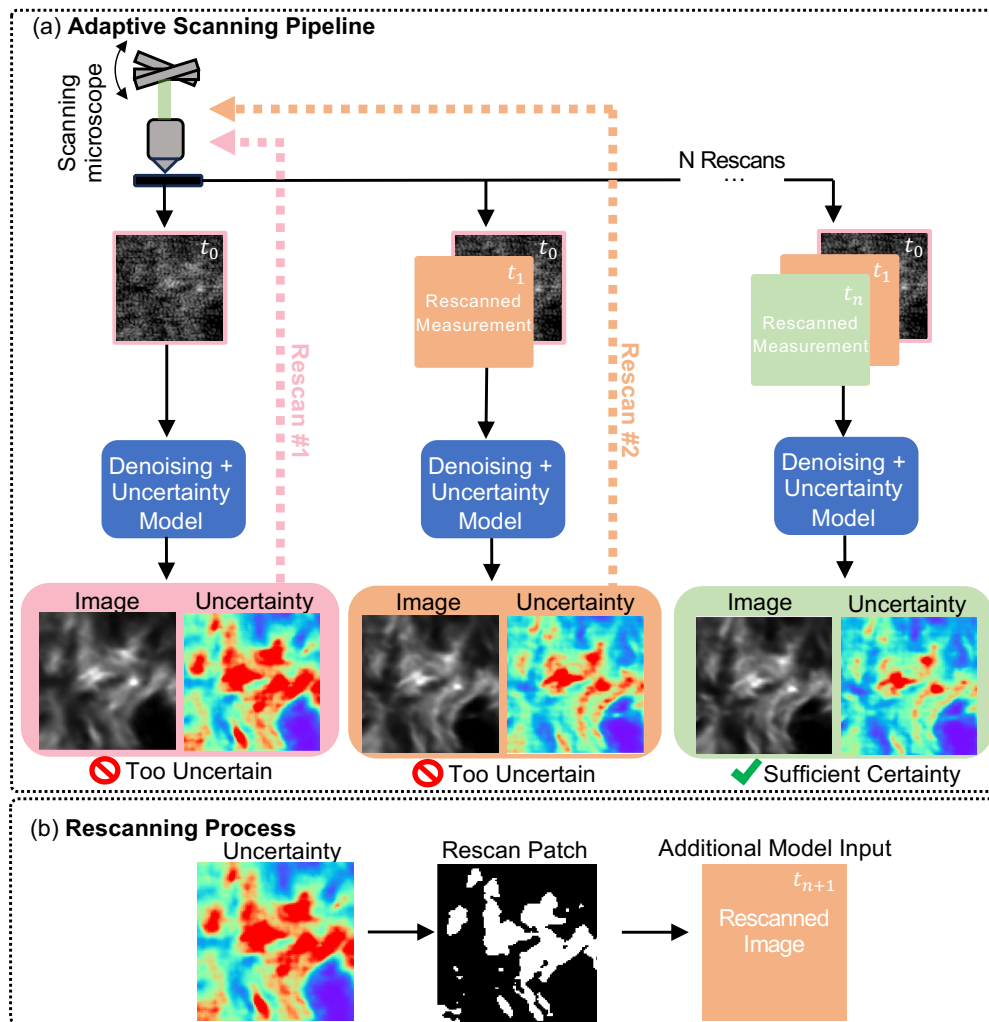


Fig. 1. (a) **Uncertainty-based Adaptive Imaging**: A noisy measurement is acquired with a scanning multiphoton microscope (MPM) and passed into a deep learning model that predicts a denoised image and its associated pixel-wise uncertainty. Subsequently, the top N uncertain pixels are selected for a rescan, obtaining more measurements at only the uncertain regions. As more adaptive measurements are taken, the deep learning model predicts a denoised image with lower uncertainty. Scan duration and power are minimized, limiting sample damage while maintaining high confidence in the model prediction. (b) **Rescanning Process**: Given a pixel-wise uncertainty prediction, regions with high uncertainty can be selected for rescanning. Only this patch of pixels will be rescanned in the sample, and this patch, superimposed with the original, becomes an additional channel that is fed into the model.

thick and living samples [18]. Since most MPM systems rely on point scanning, there is an inherent trade-off between acquisition time, field of view (FOV), phototoxicity, and image quality, often resulting in noisy measurements when fast, large FOV, deep, and/or gentle imaging is needed. Noisy images can be challenging to interpret, and fine structures within the images can be obscured by noise.

Deep learning (DL) based methods have shown exciting results for denoising extremely noisy images in microscopy [19–21]. Specifically for MPM, deep learning methods have demonstrated faster scan times and improved image quality [22–26]. Despite the success of DL, there is still a lot we do not understand, and the robustness of deep learning-based methods has been called into question [27]. Specifically, DL methods have been shown to hallucinate [28–30], i.e., produce realistic-looking artifacts that are not truly present in the sample, and suffer from instabilities, i.e., sensitivity to small perturbations in the measurement [27]. Hallucination may be acceptable or even desirable for photography or image generation but is unacceptable for biomedical and scientific imaging, where small image features may lead to important diagnoses or discoveries. To be adopted for scientific and medical imaging, deep learning methods need to be robust and trustworthy.

Uncertainty quantification techniques can help catch model hallucinations and improve the robustness of deep learning methods. Typically, a deep learning model will be trained using image pairs (e.g., noisy and noiseless), and then, at test time, given a measurement, the model will produce an estimate of the image. In addition to the image estimate, uncertainty quantification methods aim to produce an uncertainty map for each pixel in the image (Fig. 1). Typically, this has been accomplished with Bayesian neural networks with techniques like dropout [31–33]. More recently, conformal risk control paired with pixel-wise quantile regression has been proposed for distribution-free uncertainty quantification [34]. This method is much faster than Bayesian approaches, requiring only one forward pass at test time, and produces confidence sets backed by rigorous statistical guarantees.

In our work, we demonstrate distribution-free uncertainty quantification for MPM denoising and propose an adaptive microscopy imaging pipeline informed by uncertainty quantification (Fig. 1). To incorporate uncertainty quantification into any supervised deep denoising method, we need to make two simple modifications: we modify the network to predict a lower bound and upper bound for each image (i.e. quantile regression) and use a post-training calibration step to properly scale our learned uncertainty interval so that it contains the correct fraction of ground truth pixels based on a held-out calibration dataset (i.e. conformal risk control), (Fig. 2) [34, 35]. With these modifications, a denoiser will predict not only a denoised image but also a confidence interval for each pixel with a statistical guarantee that a percentage of the true values will fall within this interval. From this confidence interval, we can identify regions of our denoised image with the highest uncertainty, which can be caused by uncertainty in the model or signal. Having a confidence interval with statistical guarantees that the true signal intensity lies within these bounds is a significant advance towards making deep-learning-based denoising methods trustworthy enough for scientific and medical MPM imaging.

Taking it one step further, we propose to leverage the learned uncertainty to drive adaptive acquisition: we capture more measurements of our sample *only* at the most uncertain regions rather than rescanning the whole sample. Thus, we first capture a single noisy scan (fast and minimal sample damage due to low power or dwell time), followed by denoising, and then repeated adaptive scanning of the most uncertain regions. This way, we can leverage signal across multiple frames to improve denoising performance and reduce uncertainty while minimizing scan duration and damage to the sample. Our proposed adaptive acquisition is both sample and algorithm-informed; i.e., we acquire more measurements in locations where our denoising algorithm is struggling in order to resolve finer features, reduce hallucinations, and improve overall confidence in the image prediction.

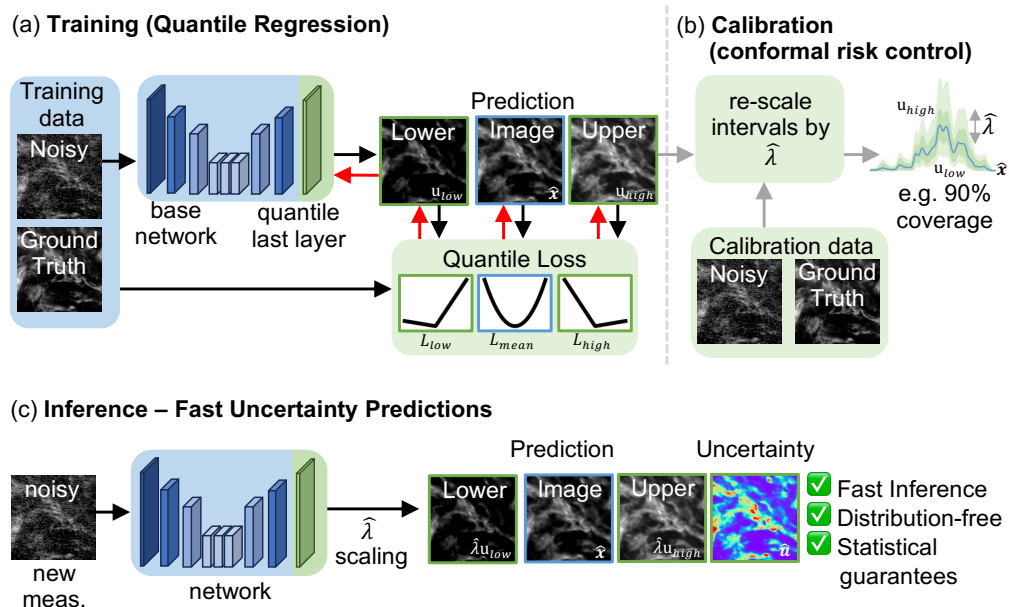


Fig. 2. **Learned Uncertainty Quantification:** To leverage distribution-free uncertainty quantification with a deep network, three modifications are needed: a last layer that predicts a lower and upper bound, a modified loss, and a post-training calibration step. Standard deep denoising steps are highlighted in blue, while our modifications are highlighted in green. (a) During training, the modified network returns three channels: the lower uncertainty quantile, the denoised prediction, and the upper uncertainty quantile. A quantile loss function defines the loss for the upper and lower quantiles, encouraging underestimates and overestimates. (b) After training, a calibration step is needed to adjust the upper and lower bounds and provide statistical guarantees for this predicted interval. (c) At test time, a single forward pass determines the uncertainty at each step, which is the difference between the upper and lower quantile predictions.

We demonstrate our adaptive acquisition approach on representative experimental data based second harmonic generation (SHG, one type of label-free MPM), showing that we can decrease total scanning time and light dose by 120 \times while recovering fine features in the sample. Furthermore, our method successfully predicts uncertainty at each pixel while outperforming other denoising methods, which do not predict uncertainty. To the best of our knowledge, we are the first to demonstrate distribution-free uncertainty quantification for a denoising task with real experimental data and the first to propose adaptive acquisition based on reconstruction uncertainty.

2. Related Work

2.1. Multiphoton microscopy

Multiphoton (MPM) microscopy has been increasingly utilized in the biomedical field due to its ability to achieve three-dimensional subcellular resolution and deep tissue penetration. MPM relies upon the nonlinear interaction between ultrafast optical pulses and fluorophores, molecular structures, and vibrational bonds of molecules [15, 36–40]. Here, we use nonlinear contrast from SHG as a demonstrative example to illustrate the advantages and practicality of our proposed methodology for photon-starved point scanning image applications. SHG signal occurs for phase-matched non-centrosymmetric structures, enabling high-resolution imaging of collagen and muscle fibers in thick and unlabeled tissues [9, 41]. SHG imaging has been widely used to characterize the reorganization of extracellular matrix in breast cancer, ovarian cancer, and

wound healing. We test our adaptive microscopy technique on SHG; however, we believe this framework could easily be adapted to other photon-starved point scanning imaging applications, including confocal microscopy, multiphoton fluorescence imaging, and coherent Raman imaging.

2.2. Denoising

A variety of denoising techniques have been proposed throughout the years. Classic denoising methods rely on hand-picked priors and heuristic design, such as sparsity [42], smoothness, or patch similarity [43]. These methods have been surpassed by data-driven methods (e.g., dictionary learning and deep learning), in which an image prior is learned from training data. Deep learning-based methods have achieved remarkable performance for denoising, but their performance depends on the noise and image distributions seen during training. Often, simplistic noise assumptions are used (e.g., iid Gaussian), and unsurprisingly, it's been shown that classic methods can outperform deep methods on real measurements with real noise [44]. Because DL methods learn to denoise measurements with a specific noise and signal distribution, they underperform on measurements outside their dataset. While classic methods can be more general, deep methods are specific and trade accuracy for stability [45]. Training from scratch or fine-tuning models with experimentally captured data can mitigate some of this and improve performance for specific noise and image distributions. In this work, we utilize supervised denoising but incorporate learned uncertainty quantification to improve the trustworthiness of denoised predictions for scientific applications.

Another line of work focuses on unsupervised or self-supervised denoising. These methods bypass the need for real training data, instead using the network structure as a prior [46] or statistical independence of noise and correlation of signal across an image [47, 48] to denoise unpaired noisy measurements. While these methods are promising, they are often surpassed by supervised methods in terms of image quality and computational time.

Specifically for low-light measurements with poor SNR, leveraging multiple frames rather than a single frame during denoising can improve performance since each measurement will have correlated signal but uncorrelated noise. Burst denoising, in which multiple noisy frames are used to estimate a single noiseless image, is used for nighttime photography on smartphones [49]. Similarly, leveraging multiple frames for video denoising has demonstrated impressive results in extreme low light conditions [50]. We take inspiration from burst denoising methods to develop an adaptive scanning approach that adaptively acquires new measurements to improve our denoising performance and reduce uncertainty.

2.3. Uncertainty quantification methods

Uncertainty quantification for deep learning is an active area of interest, and is particularly critical for leveraging machine learning models in physics, science, and medical imaging [32, 51]. The most popular methods are based on Bayesian statistics, including methods such as Bayesian networks and Monte Carlo dropout [31, 52, 53], or are ensemble-based [54], i.e. training multiple networks as a proxy for uncertainty. However, these methods have two main issues: they cannot provide strong statistical guarantees (a.k.a. they cannot guarantee how reliably they evaluate the true variability of the underlying data distribution, often requiring accurate distribution priors) [55, 56], and are often computationally intensive, requiring multiple passes through a network at test time. More recently, distribution-free uncertainty quantification based on conformal risk control have been proposed as an alternative to Bayesian methods for uncertainty quantification in deep networks [34, 57, 58]. This approach predicts pixel-wise uncertainty intervals for each image with a user-specified confidence probability. This method is agnostic to model or data distributions, provides formal mathematical guarantees, and is computationally inexpensive. We leverage distribution-free uncertainty quantification for MPM denoising, evaluating its performance on a challenging experimental denoising problem for the first time.

2.4. Adaptive acquisition in microscopy

A number of adaptive acquisition techniques have been proposed to reduce overall light dose, reduce scanning time, or enhance weak signals in microscopy [59–62]. Many of these methods rely on detecting the sample or regions of interest, either by a coarse prescan [60] or real-time specimen tracking [63, 64]. Several event-driven approaches have been proposed that adapt the acquisition from a slow imaging rate to a faster imaging rate after detecting an event either heuristically [65] or with a neural network trained to detect precursors to events [66]. In addition, machine learning techniques have been utilized to optimize the excitation power for a 3D sample in MPM [67]. While previous methods decouple the adaptive acquisition from any reconstruction algorithms (or lack thereof), our method is distinct in that we tightly couple the adaptive acquisition and the reconstruction algorithm. Our adaptive acquisition is driven by uncertainty in our denoising algorithm, with each additional measurement improving the algorithm’s performance. This allows us to push the trade-offs of light dose, speed, and imaging quality by adaptive imaging at low signal levels while algorithmically recovering a high-fidelity signal.

3. Methods

Our goal is to predict a noiseless image and its uncertainty given one or several measurements that are corrupted by noise. Assuming our sample is non-moving, our measurements can be described as:

$$\mathbf{y}_t = n_t(\mathbf{x}), \quad (1)$$

where each measurement \mathbf{y}_t contains the signal, \mathbf{x} , which is measured through some noise function $n_t(\cdot)$. Our denoiser, F_θ , predicts both the denoised image and the uncertainty at each pixel

$$\hat{\mathbf{x}}_T, \hat{\mathbf{u}}_T = F_\theta(\mathbf{y}_0, \dots, \mathbf{y}_T). \quad (2)$$

For single-image denoising, the denoiser uses a single measurement, \mathbf{y}_0 . For multi-image denoising, the denoiser uses T measurements $\mathbf{y}_0, \dots, \mathbf{y}_T$. Using multiple measurements improves the prediction and reduces uncertainty at each pixel. We can use our denoiser as is to obtain a denoised image and uncertainty estimate, or we can use the uncertainty to drive our scanning process for adaptive microscopy.

For adaptive microscopy, we take a preliminary scan of the sample, then feed this measurement into the denoiser to obtain the initial image and uncertainty estimates, $\hat{\mathbf{x}}_0, \hat{\mathbf{u}}_0 = F_\theta(\mathbf{y}_0)$. The uncertainty estimate at each pixel is used to determine which locations in the sample to rescan next:

$$(\mathbf{r}_{t+1}, \mathbf{c}_{t+1}) = A(\hat{\mathbf{u}}_t), \quad (3)$$

where r and c represent the rows and columns of the locations in the sample. Thus, the uncertainty estimate at time t determines the pixels to scan at time $t + 1$. The most uncertain areas of the sample are rescanned to obtain the next measurement, $\mathbf{y}_{t+1}(\mathbf{r}_{t+1}, \mathbf{c}_{t+1})$. The function $A(\cdot)$ defines our re-sampling strategy based on the pixel-wise uncertainty. The simplest update strategy is to rescan pixels above a certain uncertainty threshold. A more sophisticated update strategy would consider the dynamics and physical constraints of the scanning hardware, for example, rescanning rows at a time rather than random-access pixels.

With this adaptive microscopy approach, we rescan only the most uncertain positions in our sample, saving time and reducing photodamage to our sample. With each subsequent scan, the fidelity of our denoised image estimate improves, and our uncertainty decreases, meaning

we need to rescan fewer positions each time. In the following sections, we detail how to add uncertainty quantification into a denoising network and how we design the update rules for adaptive microscopy.

3.1. Learning uncertainty through quantile regression

Our adaptive microscopy method is based on rescanning the most uncertain regions of the sample, but how do we know where the most uncertain regions are? In this work, we use pixel-wise quantile regression as a metric for uncertainty [35]. Given a deep network, we add a modified last layer to the network that returns two additional channels: the lower bound (\mathbf{u}_{low}) and the upper bound (\mathbf{u}_{high}) for each predicted pixel, Fig. 2. These bounds form a confidence interval for our image estimate and provide a notion of uncertainty at each pixel. If we want 90% coverage, i.e., a 90% probability that our confidence interval will include the true value, we can set the upper and lower bounds to be the 95% quantile and 5% quantile, respectively.

To have our network predict the upper and lower quantiles, we use a quantile loss during training. The quantile loss is defined as:

$$L_q(\mathbf{x}^i, \hat{\mathbf{x}}^i) = \begin{cases} q \cdot |\mathbf{x}^i - \hat{\mathbf{x}}^i| & \text{if } \mathbf{x}^i - \hat{\mathbf{x}}^i \geq 0 \\ (1 - q) \cdot |\mathbf{x}^i - \hat{\mathbf{x}}^i| & \text{otherwise,} \end{cases} \quad (4)$$

where q is the desired quantile, ranging from 0 to 1. This loss function is asymmetric (see Fig. 2); if $q > 0.5$, underestimates are penalized heavily, and if $q < 0.5$, overestimates are penalized heavily. For our training model, we used $q_{\text{low}} = 0.05$ and $q_{\text{high}} = 0.95$ to obtain 90% coverage for our confidence interval. These values can be adjusted to obtain higher or lower coverage.

While quantile loss is used for the upper and lower bound images, any standard image loss can be used for image prediction (e.g., MSE, L1, LPIPS). Here, we use mean squared error (MSE) as the loss function for the image prediction and quantile loss for the lower and upper bounds. Training our denoising and learned uncertainty quantification network can be summarized as solving the following optimization problem:

$$\min_{\theta} \sum_i L_{q_{\text{low}}}(\mathbf{x}^i, \hat{\mathbf{u}}_{\text{low}}^i) + L_{\text{mean}}(\mathbf{x}^i, \hat{\mathbf{x}}^i) + L_{q_{\text{high}}}(\mathbf{x}^i, \hat{\mathbf{u}}_{\text{high}}^i). \quad (5)$$

Where $\hat{\mathbf{x}}^i = F_{\theta}(\mathbf{y}_0^i, \dots, \mathbf{y}_T^i)$ is the predicted denoised image and $L_{\text{mean}}(\mathbf{x}^i, \hat{\mathbf{x}}^i) = \|\mathbf{x}^i - \hat{\mathbf{x}}^i\|_2^2$ is the loss on the image prediction channel. Here, $(\mathbf{x}^i, \mathbf{y}_0^i, \dots, \mathbf{y}_T^i)$ corresponds to image pairs within our training dataset consisting of one ground truth image for each set of noisy measurements, with a total of N pairs. After training, our network, F_{θ} , produces a lower bound, image prediction, and upper bound.

3.2. Calibrating Uncertainty through Conformal Risk Control

Now, we have an uncertainty interval at each pixel, but can we trust it? This is where conformal risk control comes in [34, 57]. With conformal risk control, a held-out calibration dataset is used to assess and calibrate the uncertainty intervals. This calibration step is distribution-free, meaning it does not rely on any assumptions about the distribution of our dataset or model. During calibration, the lower and upper bounds, $(\hat{\mathbf{u}}_{\text{low}}, \hat{\mathbf{u}}_{\text{high}})$, are scaled by $\hat{\lambda}$ until they contain the correct fraction of ground truth pixels based on the calibration dataset. The final pixel-wise uncertainty is:

$$\hat{\mathbf{u}} = \hat{\lambda}(\hat{\mathbf{u}}_{\text{high}} - \hat{\mathbf{u}}_{\text{low}}). \quad (6)$$

To determine $\hat{\lambda}$, we select a maximum allowable percentage of incorrect values, α , where α ranges between 0 and 1 (e.g., 0.1 means our set will contain 90% of the true values). Given a

user-specified α , we can use the following algorithm to choose $\hat{\lambda}$:

$$\hat{\lambda} = \inf \left\{ \lambda : \hat{R}(\lambda) \leq \alpha - \frac{1 - \alpha}{N} \right\}, \quad (7)$$

where $\hat{R}(\lambda) = \frac{1}{N} \sum_{i=1}^N \frac{\text{\# of pixels miscovered in image } i \text{ when using } \lambda}{\text{total \# pixels in image } i}$. This gauges the predictive risk associated with the chosen λ by calculating the number of pixels that are not within the confidence interval given λ . The choice of $\hat{\lambda}$ statistically guarantees that the confidence interval will cover $1 - \alpha$ fraction of future pixels, given that the calibration set and new test data points are exchangeable.

$$\mathbb{E} \left[\frac{\text{\# of pixels correctly covered in new test image } i \text{ using } \hat{\lambda}}{\text{total \# of pixels in new test image } i} \right] \geq 1 - \alpha. \quad (8)$$

Since there is a difference in the distribution between a single measurement and multiple measurements for burst denoising, we must calibrate $\hat{\lambda}$ for each case independently.

3.3. Uncertainty-driven Adaptive acquisition

Pixel-wise uncertainty is used to drive our adaptive microscopy scans. Given an initial measurement at time t , our model predicts the denoised image and its associated uncertainty, \mathbf{u}_t . To choose which coordinates to rescan at time $t+1$, we select coordinates within the image that have an uncertainty above the threshold u_{thresh} . Towards this end, let $\mathcal{I}_{t+1} = \{(r, c) : \mathbf{u}_t(r, c) \geq u_{\text{thresh}}\}$ be the set of all coordinates whose uncertainty is larger than the threshold. The set \mathcal{I}_t specifies the coordinate vectors fully, and they can be rewritten as

$$\begin{aligned} \mathbf{r}_{t+1} &= (\mathcal{I}_{t+1}(0)(0), \dots, \mathcal{I}_{t+1}(n_{t+1})(0)) \\ \mathbf{c}_{t+1} &= (\mathcal{I}_{t+1}(0)(1), \dots, \mathcal{I}_{t+1}(n_{t+1})(1)), \end{aligned} \quad (9)$$

where n_{t+1} represents the cardinality of \mathcal{I}_{t+1} .

Thus, we only rescan the most uncertain pixels within the sample (Fig. 1b), with the uncertainty at time t driving the adaptive scan at time $t+1$. In each subsequent pass, the model takes in the original noisy measurement and superimposed rescans to perform multi-image denoising. With each pass, our model has more data at the uncertain pixels and can improve its image prediction and confidence. This iterative process increases the number of observations at the most uncertain positions within the sample until the model's prediction is within an acceptable uncertainty level (Fig. 1a). In practice, this process is limited by the fixed, finite input size of the denoiser. In our case, we choose the network input size to be five and are therefore limited to four total adaptive rescans. Note that the statistical guarantees from conformal risk control apply only to the first round of scanning — the guarantee is formally lost after multiple rounds of interval construction due to the distribution shift from adaptive scanning, but we find the practical effect of this to be limited.

4. Implementation details

We tested our uncertainty quantification and adaptive acquisition technique on challenging real experimental data of a fixed human uterus under SHG. We collected an experimental dataset of noisy (low power, short dwell time) scans and corresponding ground truth (averaged longer dwell time) scans to train our denoising network. We repeated our noisy scans sequentially and used these sequential scans to test our adaptive acquisition scheme synthetically without implementing adaptive acquisition in hardware.

4.1. Sample Preparation

The samples used for imaging in this paper were fixed bulky human uterus tissue. The sample was stored in 4% Paraformaldehyde (PFA) solution at 4 °C after hysterectomy surgery. All participants provided informed consent in accordance with a protocol approved by the Partners Human Research Committee and the Massachusetts Institute of Technology Committee on the Use of Humans as Experimental Subjects (Protocol number IRB-P001994).

4.2. Data Acquisition

Images used for training and testing were acquired using a custom-built inverted scanning microscope. The microscope used a pair of galvanometer mirrors (ScannerMAX Saturn-5 Galvo and Saturn-9 Galvo) to scan the beam, and the beam was focused by a water immersion objective (Olympus XLPLN25XWMP2, 1.05 NA). Specifically, for the SHG images, 900 nm was selected as the excitation wavelength from a commercial OPA (Light Conversion Cronus-3P) with 1 MHz repetition rate, coupled with the corresponding emission filter (Semrock FF02-447/60-25) before being detected by the photomultiplier tube (Hamamatsu H16201-40). The microscope was controlled by custom-written software, where the images were acquired with a 300- μm field of view and a pixel dwelling time of 1 μs for noisy images. The ground truth images were obtained by averaging twenty measurements with a pixel dwelling time of 20 μs . The power at the focal plane was around 5 mW. To collect our dataset, we imaged 100 sites within a sample with 20 noisy images and one ground truth per site. Our final SHG dataset had 6 sites for testing, 82 sites, and 12 calibration sites.

4.3. Training Details

We used NAFNet [68] as our base denoising network with a few modifications. First, we modified the last layer of our network as detailed in Angelopoulos 2022 [34] to produce the upper and lower quantile images (Fig. 2). The model was modified to take five channels as an input, allowing for adaptive scanning of up to five images. The Smartphone Image Denoising Dataset (SID) [69] and the Fluorescence Microscopy Dataset (FMD) [23] were used for pre-training, with 30608 and 47980 training images, respectively. The model was pre-trained for 20 epochs on the two datasets, using an Adam optimizer with an initial learning rate of 1e-3 and a cosine annealing learning rate schedule. Additional finetuning on our model was conducted with our SHG dataset for 77 epochs. After training, we calibrated the uncertainty interval using conformal risk control and our calibration SHG dataset, as explained in Sec. 3.2. We set $\alpha = 0.1$ to select a 90% confidence interval, finding $\hat{\lambda}=1.64$, $\hat{\lambda}=1.80$, $\hat{\lambda}=1.72$ for 1, 3, and 5 images respectively. To highlight darker regions and features within our images, we display results with a gamma correction of value 2.2 for all images (measurements, denoised, ground truth), excluding uncertainty images (images with a red and blue colormap)

5. Results and Evaluation

First, we compare our denoising performance against several baselines, including both classic and deep single-image and multi-image denoisers. Next, we evaluate our denoising and uncertainty prediction as a function of the number of measurements, demonstrating the advantages of multi-image denoising for both image quality and predicted uncertainty. Finally, we evaluate our uncertainty-driven adaptive acquisition technique, testing the performance against single and multi-image acquisition and quantifying the time and light-dose benefits.

5.1. Evaluating Single and Multi-Image Denoising Performance

We evaluated our fine-tuned NAFNet model with learned uncertainty against BM3D (classical method), Noise2Self (self-supervised DL method), and pre-trained NAFNet (supervised DL

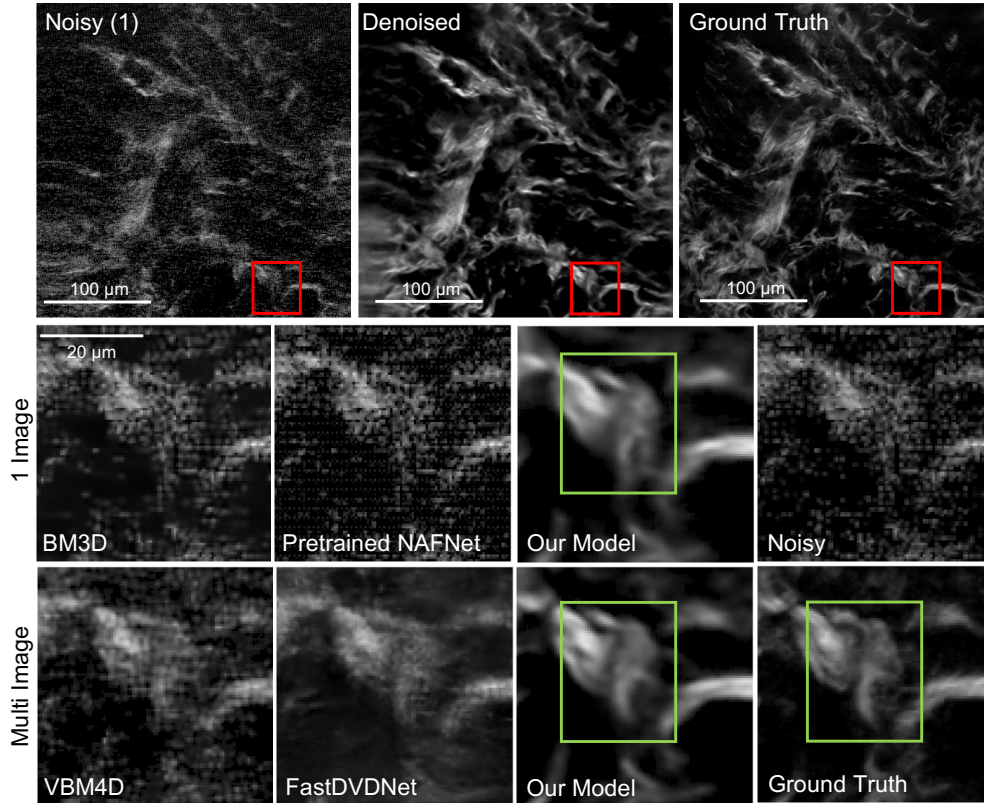


Fig. 3. **Single and Multi-Image Denoising:** Denoising results for a noisy SHG measurement. We compare single-image denoising (middle row) against multi-image denoising (bottom row). Our method outperforms BM3D (classic method) and pre-trained NAFNet (deep method) for single-image denoising. For multi-image denoising, which uses five noisy measurements for one denoised prediction, our method outperforms VBM4D (classic method) and FastDVDNet (deep method). Our multi-image model recovers more fine features within the sample, more closely matching the ground truth than the other methods or our single-image method.

method) for single-image denoising. Our method, which is fine-tuned with our SHG dataset, outperforms the other methods in terms of MSE and SSIM. Interestingly, BM3D outperforms the off-the-shelf pre-trained networks, which do not generalize well to our data distribution. However, BM3D blurs out features within the sample, causing fine details to be lost. (Table. 1). Our fine-tuned model can reconstruct features that BM3D and its pre-trained version cannot. In the region highlighted by the green box, our model recovers fine structures present in the ground truth that the other methods cannot (Fig. 3).

Since leveraging multiple image measurements could enhance a model’s overall performance, next we compare denoising performance against several multi-frame denoisers. To measure performance, we chose VBM4D (classic method) and FastDVDNet (deep method) as reference benchmarks for denoising sequences of frames. When comparing denoised results, it is evident that all the multi-image techniques outperform their single-image counterparts as expected. However, our model can recover more fine features, corroborated by the SSIM and MSE metrics. Examining the regions highlighted within the green box (refer to Fig. 3), our model produces denoised images with sharper and more discernible features, demonstrating our model’s overall superior performance.

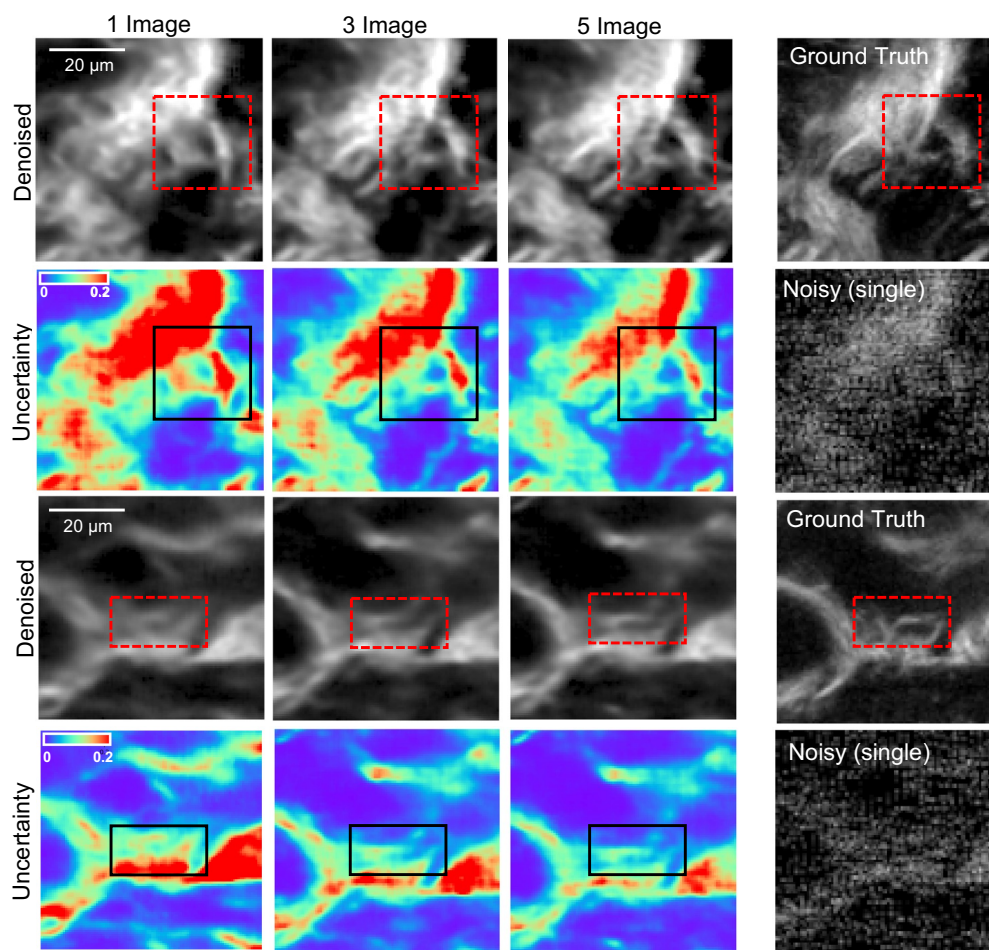


Fig. 4. **Increasing measurements reduces uncertainty:** Results of single-image, three-image, and five-image denoising, showing the image prediction and predicted uncertainty. As the number of measurements increases, the predicted image more closely matches the ground truth, and the pixel-wise uncertainty decreases.

Method	Single Image Denoising			Multi-Image Denoising (5 images)		
	MSE (1e-2) ↓	SSIM ↑	Uncertainty ↓	MSE (1e-2) ↓	SSIM ↑	Uncertainty ↓
BM3D/VBM4D	0.19 +- 0.06	0.78 +- 0.02	—	0.32 +- 0.08	0.64 +- 0.05	—
Noise2Self	0.26 +- 0.03	0.39 +- 0.03	—	—	—	—
FastDVDNet	—	—	—	0.26 +- 0.09	0.74 +- 0.04	—
Pre-trained NAFNet	0.38 +- 0.11	0.66 +- 0.06	—	0.61 +- 0.08	0.27 +- 0.01	—
Ours (SIDD/SHG)	0.12 +- 0.05	0.84 +- 0.02	0.075 +- 0.09	0.10 +- 0.03	0.88 +- 0.02	0.050 +- 0.065
Ours (FMD/SHG)	0.12 +- 0.04	0.85 +- 0.02	0.056 +- 0.064	0.10 +- 0.04	0.88 +- 0.02	0.041 +- 0.047

Table 1. Performance of Denoising Models

5.2. Increasing Image Measurements decreases Predicted Uncertainty

With more measurements, the predicted uncertainty of the network decreases, demonstrating an increase in the confidence of the predicted image. We determined the display threshold for all three uncertainty predictions by choosing the uncertainty interval linked to the top 5% most uncertain pixels. Red pixel regions indicate areas with larger uncertainty, whereas pixels appearing blue represent lower uncertainty intervals. In the two different sample regions shown in Fig. 4, as the model receives more noisy measurements, its denoised predictions become sharper and closer to the ground truth. More importantly, as more fine structures are present, the uncertainty decreases. In the second row of Fig. 4, the uncertainty gradually decreases as the number of measurements increases in the region highlighted by a black box. Its corresponding denoised outputs show a triangular region that gradually becomes closer and closer in structure to the ground truth image. This finding affirms that increasing measurements to our model not only improves denoising performance but also decreases the denoised prediction’s uncertainty.

5.3. Adaptive Sample Acquisition and Uncertainty Informed Denoising

To evaluate our uncertainty-informed adaptive acquisition, we compared the denoising and uncertainty performance for several different uncertainty thresholds. After a measurement is denoised, a new acquisition pattern is chosen based on a user-defined uncertainty threshold. This is repeated for four subsequent acquisitions, each time acquiring new measurements only in the areas of the sample that are too uncertain (i.e higher than the uncertainty threshold). Figure 5 shows the results of this sweep for a representative sample from our test set. Here, we see that when the uncertainty threshold is lower (more pixels are rescanned), performance (based on MSE, SSIM, and average uncertainty) is better, but the total scanning duration is higher. When the threshold is higher and fewer than 40% of the pixels are rescanned, the performance drops and fewer features are successfully recovered. For this sample, we found that an uncertainty threshold corresponding to rescanning 57% of the sample minimizes total time and light dose while maintaining denoising performance and successfully recovering fine features within the sample.

Table 2 summarizes the total time and total light dose required to obtain the ground truth image, 5-image denoised, 1-image denoised, and adaptive acquisition at 57% rescanning, assuming an image of size 512×512. Adaptive acquisition results in a 120× improvement in total scanning time and a 120× reduction in total light dose compared to the ground truth for this particular sample. In general, the trade-off between acquisition time and performance is sample-dependent. A dense, noisy sample will likely require more pixels rescanned, corresponding to more time and light dose than a sparse sample. We do not include computational time in our total time calculations. Currently, for a 512×512 sample, the inference time is ~0.11s on a GPU to obtain both the image and uncertainty map. We are confident this could be sped up with speed-specialized hardware and algorithms, as has been demonstrated to speed up other machine learning methods [70].

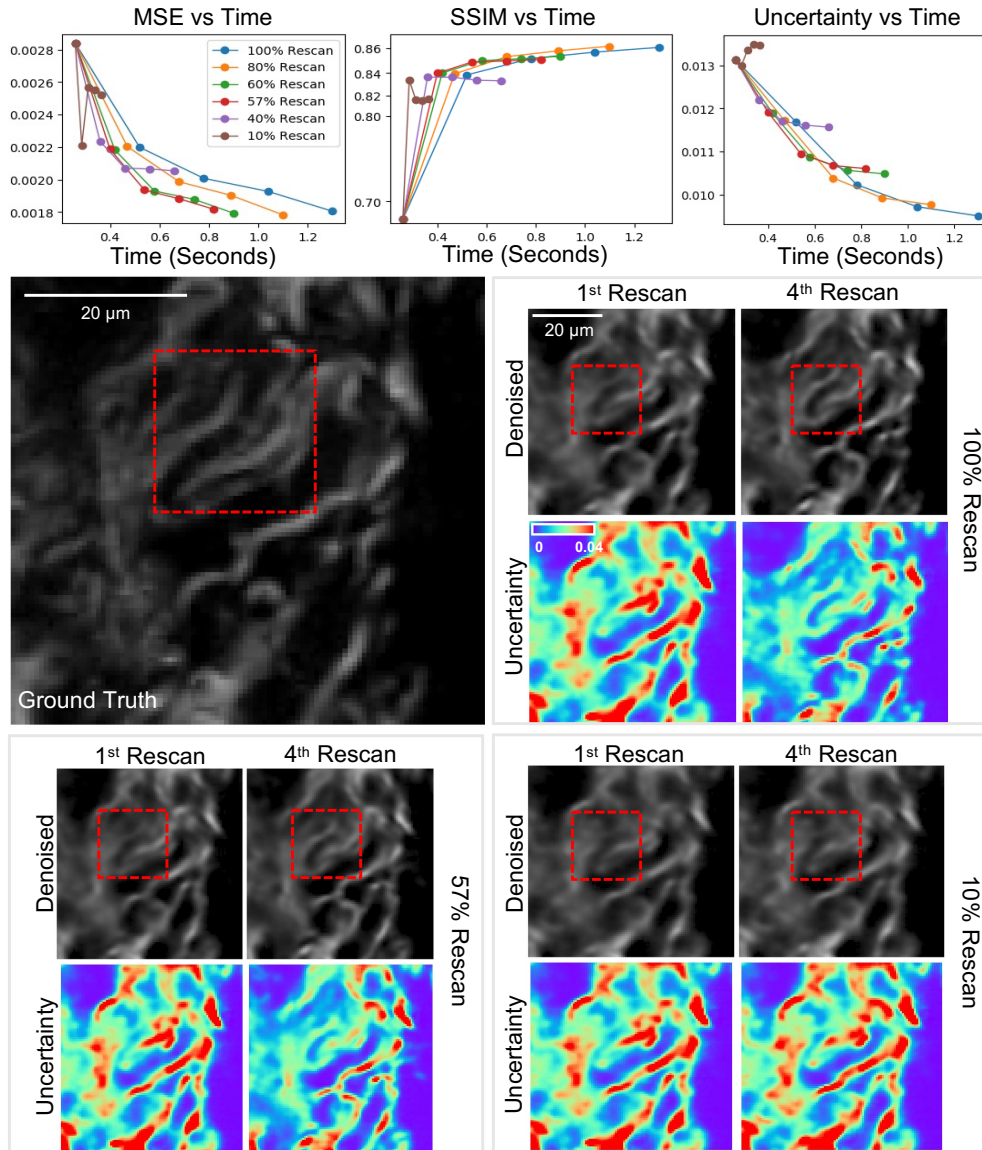


Fig. 5. **Model Performance with Adaptive Acquisition:** The MSE, SSIM, and average uncertainty are shown for a representative sample that is adaptively rescanned based on a selected uncertainty threshold, corresponding to rescanning between 10-100% of the pixels (top row). Up to a certain point, adaptive acquisition demonstrates results comparable to completely rescanning the sample, while requiring less overall imaging time. However, when rescanning falls below a threshold of 40%, denoised predictions fail to restore significant image features, and there is no noticeable change in uncertainty between acquisitions.

Measurement	Total Time (s)	Total Light Dose (mJ)	SSIM
Ground truth	104.86	524.3	—
Five noisy	1.31	6.5	0.860
Adaptive Acquisition	0.74	4.4	0.851
Single Noisy	0.26	1.3	0.838

Table 2. Time and total light dose for adaptive acquisition

6. Discussion

We presented a method to utilize learned, distribution-free uncertainty quantification for multi-image denoising and proposed an adaptive acquisition technique based on the learned uncertainty. We demonstrated both methods on experimental MPM SHG measurements, showing a $120\times$ decrease in total scanning time and a $120\times$ decrease in total light dose while successfully recovering fine structures and outperforming existing denoising benchmarks. These speed and total light dose improvements are significant and demonstrate an important step towards faster and gentler MPM, which will enable the imaging of a new class of interesting samples and lead to new scientific insights and advances.

Furthermore, we demonstrate how deep learning methods for microscopy can be designed to be trustworthy by building in uncertainty quantification to provide error bars for each prediction. To the best of our knowledge, we are the first to utilize distribution-free uncertainty quantification for a denoising task. Uncertainty quantification should become standard practice when using deep-learning techniques for scientific and medical imaging to reduce hallucinations and build confidence in image predictions. We believe that the distribution-free learned uncertainty quantification presented here is an attractive path toward this due to its ease of use, fast computational time, and statistical guarantees.

Our uncertainty-driven adaptive acquisition technique stands out from existing methods in that it is both sample and algorithm-informed. This tight coupling means that we choose to acquire new measurements not only based on the sample, but also based on how well the algorithm is performing on our measurements. To the best of our knowledge, we are the first to propose adaptive acquisition based on algorithm uncertainty. We believe this sort of technique will become widespread for efficient, adaptive computational imaging systems that design their sampling scheme in an optimal, sample and algorithm-informed way.

Limitations include that we synthetically performed adaptive acquisition by capturing multiple measurements of the same sample and digitally rescanning without actual hardware rescanning. Future directions include utilizing adaptive uncertainty-driven acquisition in-the-loop with hardware using random-access MPM or by incorporating hardware constraints to the adaptive acquisition scheme (e.g., rescanning rows instead of random access points). Other next steps include applying algorithmic-centric adaptive acquisition to 3D or moving samples and multi-modal MPM.

Acknowledgment. We would like to express our sincere gratitude to Ellen Kan, Keith Isaacson, Peter Movilla, and other staff from Newton Wellesley Hospital for facilitating the tissue collection program with MIT as well as the patients who donated their tissues for our research. Kristina Monakhova acknowledges funding from the MIT Postdoctoral Fellowship for Engineering Excellence. Cassandra Ye would like to thank the MIT EECS UROP and SUPERUROP programs for their continued support in funding. The authors acknowledge the MIT SuperCloud and Lincoln Laboratory Supercomputing Center for providing (HPC, database, consultation) resources that have contributed to the research results reported within this paper.

Data availability. Code will be available on a publicly accessible GitHub repository.

Funding.

MIT Startup Fund (KL)

MIT Postdoctoral Fellowship for Engineering Excellence (KM)

MIT EECS SuperUROP Fund (CTY)

Disclosures. The authors declare no conflicts of interest.

References

1. W. Denk, J. H. Strickler, and W. W. Webb, "Two-photon laser scanning fluorescence microscopy," *Science* **248**, 73–76 (1990).
2. G. Borile, D. Sandrin, A. Filippi, K. I. Anderson, and F. Romanato, "Label-free multiphoton microscopy: Much more than fancy images," *Int. J. Mol. Sci.* **22** (2021).
3. W. R. Zipfel, R. M. Williams, and W. W. Webb, "Nonlinear magic: multiphoton microscopy in the biosciences," *Nat. biotechnology* **21**, 1369–1377 (2003).
4. A. Attardo, J. E. Fitzgerald, and M. J. Schnitzer, "Impermanence of dendritic spines in live adult cal hippocampus," *Nature* **523**, 592–596 (2015).
5. R. Lu, W. Sun, Y. Liang, A. Kerlin, J. Bierfeld, J. D. Seelig, D. E. Wilson, B. Scholl, B. Mohar, M. Tanimoto *et al.*, "Video-rate volumetric functional imaging of the brain at synaptic resolution," *Nat. neuroscience* **20**, 620–628 (2017).
6. R. Prevedel, A. J. Verhoef, A. J. Pernía-Andrade, S. Weisenburger, B. S. Huang, T. Nöbauer, A. Fernández, J. E. Delcour, P. Golshani, A. Baltuska *et al.*, "Fast volumetric calcium imaging across multiple cortical layers using sculpted light," *Nat. methods* **13**, 1021–1028 (2016).
7. L. Perrin, B. Bayarmagnai, and B. Gligorijevic, "Frontiers in intravital multiphoton microscopy of cancer," *Cancer Reports* **3**, e1192 (2020).
8. S. You, E. J. Chaney, H. Tu, Y. Sun, S. Sinha, and S. A. Boppart, "Label-free deep profiling of the tumor microenvironment," *Cancer research* **81**, 2534–2544 (2021).
9. C. G. Fuentes-Corona, J. Licea-Rodriguez, R. Younger, R. Rangel-Rojo, E. O. Potma, and I. Rocha-Mendoza, "Second harmonic generation signal from type I collagen fibers grown in vitro," *Biomed. optics express* **10**, 6449–6461 (2019).
10. D. Débarre, W. Supatto, A.-M. Pena, A. Fabre, T. Tordjmann, L. Combettes, M.-C. Schanne-Klein, and E. Beaupaire, "Imaging lipid bodies in cells and tissues using third-harmonic generation microscopy," *Nat. methods* **3**, 47–53 (2006).
11. Y. Barad, H. Eisenberg, M. Horowitz, and Y. Silberberg, "Nonlinear scanning laser microscopy by third harmonic generation," *Appl. Phys. Lett.* **70**, 922–924 (1997).
12. W. R. Zipfel, R. M. Williams, R. Christie, A. Y. Nikitin, B. T. Hyman, and W. W. Webb, "Live tissue intrinsic emission microscopy using multiphoton-excited native fluorescence and second harmonic generation," *Proc. National Acad. Sci.* **100**, 7075–7080 (2003).
13. A. Periasamy, K. König, and P. So, "Special section guest editorial: Thirty years of multiphoton microscopy in the biomedical sciences," *J. Biomed. Opt.* **25** (2020).
14. A. C.-H. Chen, C. McNeilly, A. P.-Y. Liu, C. J. Flaim, L. Cuttle, M. Kendall, R. M. Kimble, H. Shimizu, and J. R. McMillan, "Second harmonic generation and multiphoton microscopic detection of collagen without the need for species specific antibodies," *Burns* **37**, 1001–1009 (2011).
15. M. C. Skala, K. M. Riching, A. Gendron-Fitzpatrick, J. Eickhoff, K. W. Eliceiri, J. G. White, and N. Ramanujam, "In vivo multiphoton microscopy of nadh and fad redox states, fluorescence lifetimes, and cellular morphology in precancerous epithelia," *Proc. National Acad. Sci.* **104**, 19494–19499 (2007).
16. E. B. Brown, R. B. Campbell, Y. Tsuzuki, L. Xu, P. Carmeliet, D. Fukumura, and R. K. Jain, "In vivo measurement of gene expression, angiogenesis and physiological function in tumors using multiphoton laser scanning microscopy," *Nat. medicine* **7**, 864–868 (2001).
17. S. You, H. Tu, E. J. Chaney, Y. Sun, Y. Zhao, A. J. Bower, Y.-Z. Liu, M. Marjanovic, S. Sinha, Y. Pu *et al.*, "Intravital imaging by simultaneous label-free autofluorescence-multiphoton microscopy," *Nat. communications* **9**, 2125 (2018).
18. G. Volpe, C. Wählby, L. Tian, M. Hecht, A. Yakimovich, K. Monakhova, L. Waller, I. F. Sbalzarini, C. A. Metzler, M. Xie *et al.*, "Roadmap on deep learning for microscopy," *ArXiv* (2023).
19. M. Weigert, U. Schmidt, T. Boothe, A. Müller, A. Dibrov, A. Jain, B. Wilhelm, D. Schmidt, C. Broaddus, S. Culley *et al.*, "Content-aware image restoration: pushing the limits of fluorescence microscopy," *Nat. methods* **15**, 1090–1097 (2018).
20. J. Platasa, X. Ye, A. M. Ahrens, C. Liu, I. A. Chen, I. G. Davison, L. Tian, V. A. Pieribone, and J. L. Chen, "High-speed low-light in vivo two-photon voltage imaging of large neuronal populations," *Nat. Methods* pp. 1–9 (2023).
21. L. von Chamier, R. F. Laine, J. Jukkala, C. Spahn, D. Krentzel, E. Nehme, M. Lerche, S. Hernández-Pérez, P. K. Mattila, E. Karinou *et al.*, "Democratising deep learning for microscopy with zerocostdl4mic," *Nat. communications* **12**, 2276 (2021).
22. C.-W. Hsu, C.-Y. Lin, Y. Y. Hu, C.-Y. Wang, S.-T. Chang, A.-S. Chiang, and S.-J. Chen, "Three-dimensional-generator u-net for dual-resonant scanning multiphoton microscopy image inpainting and denoising," *Biomed. Opt. Express* **13**, 6273–6283 (2022).

23. Y. Zhang, Y. Zhu, E. Nichols, Q. Wang, S. Zhang, C. Smith, and S. Howard, "A poisson-gaussian denoising dataset with real fluorescence microscopy images," in *Proceedings of the IEEE/CVF Conference on Computer Vision and Pattern Recognition*, (2019), pp. 11710–11718.
24. S. Lee, M. Negishi, H. Urakubo, H. Kasai, and S. Ishii, "Mu-net: Multi-scale u-net for two-photon microscopy image denoising and restoration," *Neural Networks* **125**, 92–103 (2020).
25. R. F. Laine, G. Jacquemet, and A. Krull, "Imaging in focus: an introduction to denoising bioimages in the era of deep learning," *The international journal biochemistry & cell biology* **140**, 106077 (2021).
26. B. Manifold, E. Thomas, A. T. Francis, A. H. Hill, and D. Fu, "Denoising of stimulated raman scattering microscopy images via deep learning," *Biomed. optics express* **10**, 3860–3874 (2019).
27. V. Antun, F. Renna, C. Poon, B. Adcock, and A. C. Hansen, "On instabilities of deep learning in image reconstruction and the potential costs of ai," *Proc. National Acad. Sci.* **117**, 30088–30095 (2020).
28. Z. Ji, N. Lee, R. Frieske, T. Yu, D. Su, Y. Xu, E. Ishii, Y. J. Bang, A. Madotto, and P. Fung, "Survey of hallucination in natural language generation," *ACM Comput. Surv.* **55**, 1–38 (2023).
29. M. E. Helou, R. Zhou, and S. Ssstrunk, "Stochastic frequency masking to improve super-resolution and denoising networks," (2020).
30. S. Bhadra, V. A. Kelkar, F. J. Brooks, and M. A. Anastasio, "On hallucinations in tomographic image reconstruction," (2021).
31. Y. Gal and Z. Ghahramani, "Dropout as a bayesian approximation: Representing model uncertainty in deep learning," in *international conference on machine learning*, (PMLR, 2016), pp. 1050–1059.
32. M. Abdar, F. Pourpanah, S. Hussain, D. Rezazadegan, L. Liu, M. Ghavamzadeh, P. Fieguth, X. Cao, A. Khosravi, U. R. Acharya *et al.*, "A review of uncertainty quantification in deep learning: Techniques, applications and challenges," *Inf. fusion* **76**, 243–297 (2021).
33. Y. Xue, S. Cheng, Y. Li, and L. Tian, "Reliable deep-learning-based phase imaging with uncertainty quantification," *Optica* **6**, 618 (2019).
34. A. N. Angelopoulos, A. P. Kohli, S. Bates, M. Jordan, J. Malik, T. Alshaabi, S. Upadhyayula, and Y. Romano, "Image-to-image regression with distribution-free uncertainty quantification and applications in imaging," in *International Conference on Machine Learning*, (PMLR, 2022), pp. 717–730.
35. R. Koenker and G. Bassett Jr, "Regression quantiles," *conom. journal conom. Soc.* pp. 33–50 (1978).
36. C. Xu, W. Zipfel, J. B. Shear, R. M. Williams, and W. W. Webb, "Multiphoton fluorescence excitation: new spectral windows for biological nonlinear microscopy," *Proc. National Acad. Sci.* **93**, 10763–10768 (1996).
37. I. Georgakoudi, B. C. Jacobson, M. G. Muller, E. E. Sheets, K. Badizadegan, D. L. Carr-Locke, C. P. Crum, C. W. Boone, R. R. Dasari, J. Van Dam *et al.*, "Nad (p) h and collagen as in vivo quantitative fluorescent biomarkers of epithelial precancerous changes," *Cancer research* **62**, 682–687 (2002).
38. C. W. Freudiger, W. Min, B. G. Saar, S. Lu, G. R. Holtom, C. He, J. C. Tsai, J. X. Kang, and X. S. Xie, "Label-free biomedical imaging with high sensitivity by stimulated raman scattering microscopy," *Science* **322**, 1857–1861 (2008).
39. J.-X. Cheng and X. S. Xie, "Coherent anti-stokes raman scattering microscopy: instrumentation, theory, and applications," (2004).
40. X. Wang, D. Zhang, X. Zhang, Y. Xing, J. Wu, X. Sui, X. Huang, G. Chang, and L. Li, "Application of multiphoton microscopic imaging in study of gastric cancer," *Technol. Cancer Res. & Treat.* **21**, 15330338221133244 (2022).
41. P. Friedl, K. Wolf, G. Harms, and U. H. von Andrian, "Biological second and third harmonic generation microscopy," *Curr. Protoc. Cell Biol.* **34**, 4–15 (2007).
42. J. Portilla, V. Strela, M. J. Wainwright, and E. P. Simoncelli, "Image denoising using scale mixtures of gaussians in the wavelet domain," *IEEE Trans. on Image processing* **12**, 1338–1351 (2003).
43. K. Dabov, A. Foi, V. Katkovnik, and K. Egiazarian, "Image denoising by sparse 3-d transform-domain collaborative filtering," *IEEE Trans. on image processing* **16**, 2080–2095 (2007).
44. T. Plotz and S. Roth, "Benchmarking denoising algorithms with real photographs," in *Proceedings of the IEEE conference on computer vision and pattern recognition*, (2017), pp. 1586–1595.
45. N. M. Gottschling, V. Antun, B. Adcock, and A. C. Hansen, "The troublesome kernel: why deep learning for inverse problems is typically unstable," *arXiv preprint arXiv:2001.01258* (2020).
46. D. Ulyanov, A. Vedaldi, and V. Lempitsky, "Deep image prior," in *Proceedings of the IEEE conference on computer vision and pattern recognition*, (2018), pp. 9446–9454.
47. J. Batson and L. Royer, "Noise2self: Blind denoising by self-supervision," in *International Conference on Machine Learning*, (PMLR, 2019), pp. 524–533.
48. A. Krull, T.-O. Buchholz, and F. Jug, "Noise2void-learning denoising from single noisy images," in *Proceedings of the IEEE/CVF conference on computer vision and pattern recognition*, (2019), pp. 2129–2137.
49. O. Liba, K. Murthy, Y.-T. Tsai, T. Brooks, T. Xue, N. Karnad, Q. He, J. T. Barron, D. Sharlet, R. Geiss *et al.*, "Handheld mobile photography in very low light," *ACM Trans. on Graph. (TOG)* **38**, 1–16 (2019).
50. K. Monakhova, S. R. Richter, L. Waller, and V. Koltun, "Dancing under the stars: video denoising in starlight," in *Proceedings of the IEEE/CVF Conference on Computer Vision and Pattern Recognition*, (2022), pp. 16241–16251.
51. Y. Gal, P. Koumoutsakos, F. Lanusse, G. Louppe, and C. Papadimitriou, "Bayesian uncertainty quantification for machine-learned models in physics," *Nat. Rev. Phys.* **4**, 573–577 (2022).
52. A. Kendall and Y. Gal, "What uncertainties do we need in bayesian deep learning for computer vision?" *Adv. neural*

- information processing systems **30** (2017).
53. R. M. Neal, *Bayesian learning for neural networks*, vol. 118 (Springer Science & Business Media, 2012).
 54. B. Lakshminarayanan, A. Pritzel, and C. Blundell, "Simple and scalable predictive uncertainty estimation using deep ensembles," *Adv. neural information processing systems* **30** (2017).
 55. S. M. Hirsh, D. A. Barajas-Solano, and J. N. Kutz, "Sparsifying priors for bayesian uncertainty quantification in model discovery," *Royal Soc. Open Sci.* **9**, 211823 (2022).
 56. L. J. Freeman and K. Fronczyk, "Improving reliability estimates with bayesian statistics," IDA Document NS D-5452 (2015).
 57. A. N. Angelopoulos and S. Bates, "A gentle introduction to conformal prediction and distribution-free uncertainty quantification," *arXiv preprint arXiv:2107.07511* (2021).
 58. J. Teneggi, M. Tivnan, W. Stayman, and J. Sulam, "How to trust your diffusion model: A convex optimization approach to conformal risk control," in *International Conference on Machine Learning*, (PMLR, 2023), pp. 33940–33960.
 59. R. Hoebe, C. Van Oven, T. Gadella Jr, P. Dhonukshe, C. Van Noorden, and E. Manders, "Controlled light-exposure microscopy reduces photobleaching and phototoxicity in fluorescence live-cell imaging," *Nat. biotechnology* **25**, 249–253 (2007).
 60. F. Abouakil, H. Meng, M.-A. Burcklen, H. Rigneault, F. Galland, and L. LeGoff, "An adaptive microscope for the imaging of biological surfaces," *Light. Sci. & Appl.* **10**, 210 (2021).
 61. J. Dreier, M. Castello, G. Coceano, R. Cáceres, J. Plastino, G. Vicidomini, and I. Testa, "Smart scanning for low-illumination and fast resoltf nanoscopy in vivo," *Nat. communications* **10**, 556 (2019).
 62. K. K. Chu, D. Lim, and J. Mertz, "Enhanced weak-signal sensitivity in two-photon microscopy by adaptive illumination," *Opt. letters* **32**, 2846–2848 (2007).
 63. L. A. Royer, W. C. Lemon, R. K. Chhetri, Y. Wan, M. Coleman, E. W. Myers, and P. J. Keller, "Adaptive light-sheet microscopy for long-term, high-resolution imaging in living organisms," *Nat. biotechnology* **34**, 1267–1278 (2016).
 64. K. McDole, L. Guignard, F. Amat, A. Berger, G. Malandain, L. A. Royer, S. C. Turaga, K. Branson, and P. J. Keller, "In toto imaging and reconstruction of post-implantation mouse development at the single-cell level," *Cell* **175**, 859–876 (2018).
 65. J. Alvelid, M. Damenti, C. Sgattoni, and I. Testa, "Event-triggered sted imaging," *Nat. Methods* **19**, 1268–1275 (2022).
 66. D. Mahecic, W. L. Stepp, C. Zhang, J. Griffié, M. Weigert, and S. Manley, "Event-driven acquisition for content-enriched microscopy," *Nat. Methods* **19**, 1262–1267 (2022).
 67. H. Pinkard, H. Baghdassarian, A. Mujal, E. Roberts, K. H. Hu, D. H. Friedman, I. Malenica, T. Shagam, A. Fries, K. Corbin *et al.*, "Learned adaptive multiphoton illumination microscopy for large-scale immune response imaging," *Nat. communications* **12**, 1916 (2021).
 68. L. Chen, X. Chu, X. Zhang, and J. Sun, "Simple baselines for image restoration," (2022).
 69. A. Abdelhamed, S. Lin, and M. S. Brown, "A high-quality denoising dataset for smartphone cameras," in *Proceedings of the IEEE conference on computer vision and pattern recognition*, (2018), pp. 1692–1700.
 70. T. Müller, A. Evans, C. Schied, and A. Keller, "Instant neural graphics primitives with a multiresolution hash encoding," *ACM Trans. on Graph. (ToG)* **41**, 1–15 (2022).